JM PAPERS

Evidence that superstructures comprise self-similar coherent motions in high Reynolds number boundary layers

Rahul Deshpande[1,†], **Charitha M. de Silva**[2] **and Ivan Marusic**[1]

[1]Department of Mechanical Engineering, University of Melbourne, Parkville, VIC 3010, Australia
[2]School of Mechanical and Manufacturing Engineering, University of New South Wales, Sydney, NSW 2052, Australia

We present experimental evidence that the superstructures in turbulent boundary layers comprise smaller, geometrically self-similar coherent motions. The evidence comes from identifying and analysing instantaneous superstructures from large-scale particle image velocimetry datasets acquired at high Reynolds numbers, capable of capturing streamwise elongated motions extending up to 12 times the boundary layer thickness. Given the challenge in identifying the constituent motions of the superstructures based on streamwise velocity signatures, a new approach is adopted that analyses the wall-normal velocity fluctuations within these very long motions, which reveals the constituent motions unambiguously. The conditional streamwise energy spectra of the Reynolds shear stress and the wall-normal fluctuations, corresponding exclusively to the superstructure region, are found to exhibit the well-known distance-from-the-wall scaling in the intermediate-scale range. It suggests that geometrically self-similar motions are the constituent motions of these very-large-scale structures. Investigation of the spatial organization of the wall-normal momentum-carrying eddies, within the superstructures, also lends empirical support to the concatenation hypothesis for the formation of these structures. The association between the superstructures and self-similar motions is reaffirmed on comparing the vertical coherence of the Reynolds-shear-stress-carrying motions, by computing conditionally averaged two-point correlations, which are found to match with the mean correlations. The mean vertical coherence of these motions, investigated for the log region across three decades of Reynolds numbers, exhibits a unique distance-from-the-wall scaling invariant with Reynolds number. The findings support modelling of these dynamically significant motions via data-driven coherent structure-based models.

Key words: turbulent boundary layers, turbulence modelling, boundary layer control

† Email address for correspondence: raadeshpande@gmail.com

1. Introduction and motivation

Over the past two decades, the study of high Reynolds number ($Re_\tau \gtrsim O(10^4)$) wall-bounded flows has become synonymous with very-large-scale motions (VLSMs), also known as 'superstructures', which play a predominant role in the dynamics and spatial organization of wall turbulence. Here, $Re_\tau = \delta U_\tau / \nu$, where δ is the boundary layer thickness, ν is the kinematic viscosity and U_τ is the friction velocity, with the latter two used to normalize the statistics in viscous units (indicated by superscript '+'). The superstructures can extend beyond 20δ in the streamwise direction (Kim & Adrian 1999; Hutchins & Marusic 2007) and also exhibit 'meandering' when viewed on a wall-parallel plane (de Silva *et al.* 2015), particularly in the logarithmic region of the flow. Such a large spatial footprint permits these motions to carry significant proportions of the total turbulent kinetic energy and the Reynolds shear stresses of the flow (Liu, Adrian & Hanratty 2001; Guala, Hommema & Adrian 2006; Balakumar & Adrian 2007). Given that the shear stress is responsible for the wall-normal momentum transfer, this suggests that the VLSMs/superstructures also contribute significantly to the high Re_τ turbulent skin-friction drag (Deck *et al.* 2014). Hence, an improved understanding of the origin of these VLSMs/superstructures, towards which this study is directed, stands to advance our knowledge in both a fundamental and an applied perspective.

Hutchins & Marusic (2007) used the terminology 'superstructures' when referring to the spectrogram of the streamwise velocity fluctuations (u) from a high Re_τ boundary layer, as shown in figure 1. The spectrogram presents the premultiplied u-energy spectra as a function of the viscous-scaled streamwise wavelengths ($\lambda_x^+ = \lambda_x U_\tau / \nu$) and wall-normal distance ($z^+ = z U_\tau / \nu$), with $\lambda_x = 2\pi / k_x$, where k_x is the streamwise wavenumber. The high Re_τ u-spectrogram is seen to have two prominent peaks. One is located in the inner region synonymous with the well-documented near-wall cycle (Kline *et al.* 1967), consisting of high- and low-speed viscous-scaled streaks ($\lambda_x^+ \approx 1000$), which are responsible for intense local production of turbulent kinetic energy. The second peak is in the outer region of the flow (typically in the logarithmic/inertial region), and corresponds to the superstructures, which have a spectral signature at very long wavelengths ($\lambda_x \sim 6\delta$) and also extend down to the wall (Hutchins & Marusic 2007). It is worth noting here that this second peak is only visible for $Re_\tau \gtrsim 2000$, owing to the insufficient separation of scales and weaker energy of the superstructures at lower Re_τ (Hutchins & Marusic 2007). Between the inner and outer peaks, a nominal plateau is seen in the spectrogram which corresponds to the distance-from-the-wall (z)-scaled eddies coexisting in the log region; these eddies make up the increased range of scales with increasing Re_τ. In the literature, these intermediate-scaled eddies have been described by various structures or motions, including the large-scale motions (LSMs; Kim & Adrian 1999; Adrian *et al.* 2000), uniform momentum zones (Meinhart & Adrian 1995; de Silva *et al.* 2016), attached eddies (Baars, Hutchins & Marusic 2017; Marusic & Monty 2019; Hu, Yang & Zheng 2020; Deshpande, Monty & Marusic 2021*a*) and so forth. In the remainder of this section, for simplicity, we will refer to these motions as LSMs. It should also be noted that the terminology 'VLSMs' and 'superstructures' have been conventionally associated with the VLSMs in internal (Kim & Adrian 1999) and external wall-bounded flows (Hutchins & Marusic 2007), respectively. Considering this study focuses solely on zero-pressure-gradient turbulent boundary layers, we henceforth refer to either of these structures simply as superstructures.

To date, several studies have investigated the probable mechanisms responsible for the formation of superstructures, with two theories hypothesized most often: (i) the formation of superstructures via concatenation of the LSMs (Kim & Adrian 1999; Adrian *et al.* 2000;
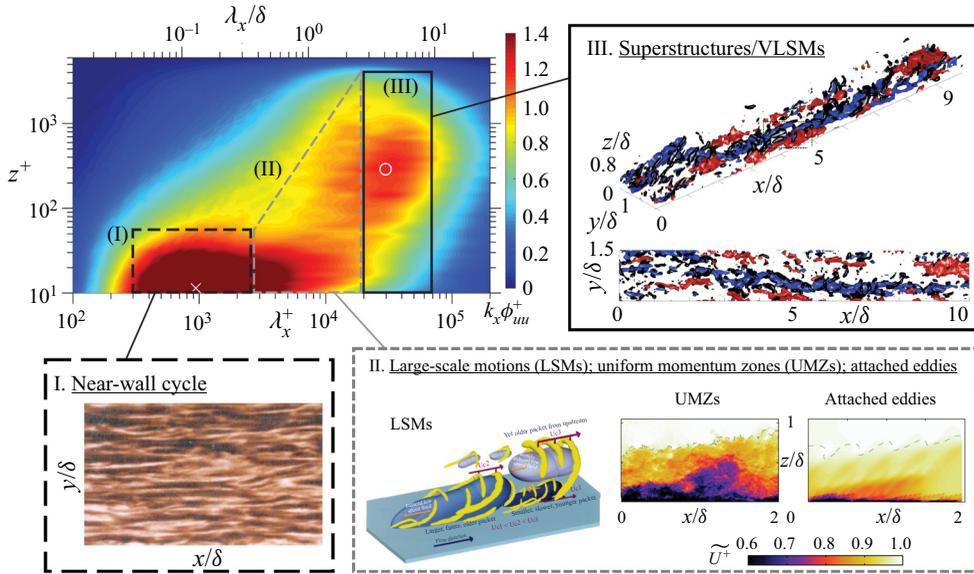
Figure 1. Premultiplied spectra of the streamwise velocity ($k_x \phi_{uu}^+$) plotted against viscous-scaled wavelength (λ_x^+) and distance from the wall (z^+) for a turbulent boundary layer at $Re_\tau \approx 7300$ (Hutchins & Marusic 2007). Here, $\times$ and $\bigcirc$ marked in the plot correspond to the 'inner' and 'outer' peaks of the u-spectrogram noted previously in the literature. Regions (I), (II) and (III) are used to indicate spectral signatures of various coherent motions observed in the literature. Region (I) corresponds to the near-wall cycle captured via flow visualization by Professor S. J. Kline (photo shared by Professor D. Coles). Region (II) corresponds to the large-scale motions (conceptual sketch by Adrian, Meinhart & Tomkins 2000), uniform momentum zones (particle image velocimetry by de Silva, Hutchins & Marusic 2016) and attached eddies (attached eddy simulations by de Silva *et al.* 2016). Region (III) corresponds to the VLSMs/superstructures, visualized via time resolved PIV by Dennis & Nickels (2011).

Dennis & Nickels 2011; Lee & Sung 2011), or (ii) the emergence of superstructures due to a linear instability mechanism (Del Alamo & Jimenez 2006; Hwang & Cossu 2010; McKeon & Sharma 2010). The present study does not focus on comparing and contrasting the likelihood of one mechanism over the other. Rather, it builds upon recent compelling evidence in support of the concatenation mechanism (Wu, Baltzer & Adrian 2012; Baltzer, Adrian & Wu 2013; Lee *et al.* 2014; Lee, Sung & Adrian 2019), to investigate the characteristics of the constituent motions forming the superstructures. The formation of superstructures via streamwise concatenation of the relatively smaller motions has been confirmed by several studies conducted across all canonical wall-bounded flows (turbulent boundary layers, channels, pipes), through: (i) investigation of the time evolution of instantaneous flow fields (Dennis & Nickels 2011; Lee & Sung 2011; Wu *et al.* 2012; Lee *et al.* 2019), (ii) statistical analysis of the superstructure formation frequency/population density (Lee *et al.* 2014) and (iii) spatial correlations of the low-pass filtered velocity fields (Baltzer *et al.* 2013; Lee *et al.* 2019). In comparison, few studies have presented similar statistical arguments in favour of the linear instability mechanism. For instance, Bailey *et al.* (2008) supported the linear instability argument by noting different spanwise widths of the superstructures and LSMs in the inertial region of a turbulent pipe flow. Their estimates, however, were limited to two-point velocity correlations reconstructed in a particular wall-parallel plane, which cannot be uniquely associated with the LSMs responsible for the superstructure formation (Deshpande *et al.* 2020). Considering that superstructures extend down from the log region to the wall, Deshpande *et al.* (2021*b*)

reconstructed two-point velocity correlations across two wall-parallel planes located in the near-wall and the log regions. These statistics, which are purely representative of the large 'wall-coherent' motions, revealed similar spanwise extents of the coexisting superstructures and LSMs for all canonical wall flows, thereby favouring the concatenation argument.

Despite substantial support for the concatenation argument, several unanswered questions are still associated with this mechanism. For instance, there is no universal agreement on what facilitates the streamwise concatenation of LSMs to form superstructures. While few studies have associated this with the spanwise alternate positioning of low- and high-momentum LSMs (Lee *et al.* 2014), others have conjectured the role played by secondary roll cells (Baltzer *et al.* 2013; Lee *et al.* 2019) in favourably organizing the relatively smaller motions. Progress in this regard has been hindered by the lack of understanding of the constituent motions forming the superstructures; for instance, are superstructures purely composed of the inertial δ-scaled motions corresponding to the extreme right end of region II in figure 1? Or do they also comprise the geometrically self-similar, i.e. z-scaled hierarchy of eddies encompassing the entirety of region II? The present study aims to answer these questions by analysing the characteristics of the constituent motions.

In the past, clarifying such information on the constituent motions has not been possible due to the low to moderate $Re_\tau (\lesssim 2000)$ of the experiments/simulations analysing the concatenation argument, which severely constricts the extent of region (II) in figure 1. This prevents an unambiguous delineation between the δ-scaled and z-scaled inertial motions coexisting in region II. Further, the statistical signature of the superstructures is also very weak at these Re_τ (Hutchins & Marusic 2007), making it challenging to identify and isolate them from the other motions in the flow. However, increased access to high Re_τ data over the past decade has substantially increased our knowledge of these inertial eddies coexisting in the log and outer regions (Marusic *et al.* 2015; Baidya *et al.* 2017; Deshpande *et al.* 2021*a*). This has also led to growing acceptance of the existence of the geometrically self-similar attached eddy hierarchy in the inertial region (de Silva *et al.* 2016; Baars *et al.* 2017; Hwang & Sung 2018; Deshpande *et al.* 2020, 2021*a*; Hu *et al.* 2020), which can be modelled conceptually (Marusic & Monty 2019). These advancements make it compelling to investigate whether these self-similar inertial motions are associated with the formation of superstructures, a conjecture that has previously shown promising results when tested for low Re_τ channel flows (Lozano-Durán, Flores & Jiménez 2012), and when implemented in coherent structure-based models (Deshpande *et al.* 2021*b*). If this conjecture is proven true, then the preferred streamwise alignment of this energy-containing hierarchy of motions (to form superstructures) would have implications for Townsend's attached eddy hypothesis, which otherwise assumes a random distribution of attached eddies in the flow field (Townsend 1976; Marusic & Monty 2019). The investigation can also help answer the long-standing contradiction (Guala *et al.* 2006; Balakumar & Adrian 2007; Wu *et al.* 2012) between: (i) the attached eddy hypothesis, which classifies turbulent superstructures to be 'inactive' (Deshpande *et al.* 2021*a*), and (ii) instantaneous flow field observations, per which these streamwise elongated motions carry significant Reynolds shear stresses (and hence behave as 'active' motions).

To this end, the present study investigates the geometric scalings exhibited by the constituent motions of the superstructures. Experimental data are employed from a moderate to high Re_τ turbulent boundary layer ($2500 \lesssim Re_\tau \lesssim 7500$), which is an order of magnitude higher than the simulation studies reported previously, to ensure coexistence of a broad range of inertial scales (region II). The dataset comprises sufficiently resolved large-scale velocity fluctuations acquired in a physically thick boundary layer via unique,
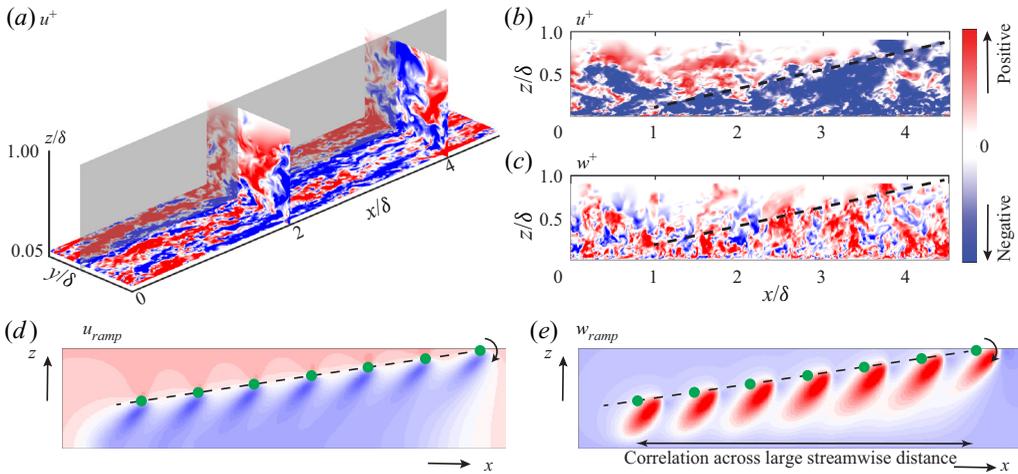
Figure 2. Colour contours of the instantaneous (*a*,*b*) streamwise, *u* and (*c*) wall-normal velocity fluctuations, *w*, in a boundary layer at $Re_\tau \approx 2000$. These data have been extracted from a particular three-dimensional (3-D) time block of the publicly available DNS dataset of Sillero, Jiménez & Moser (2013). In (*a*), *u* is plotted on a wall-parallel plane at $z \approx 0.05\delta$, as well as on the cross-planes at $x \approx 2\delta$ and 4δ. Panels (*b*) and (*c*) respectively plot the *u* and *w* fluctuations in the streamwise wall-normal plane shaded in grey in (*a*). Dashed black line in (*b*,*c*) traces the top part of a long $-u$ ramp type structure. Panels (*d*,*e*) respectively plot an idealized distribution of *u* and *w* flow field induced by multiple prograde vortices (in green) positioned along the ramp (Adrian *et al.* 2000; de Silva *et al.* 2016).

large field-of-view (LFOV) particle image velocimetry (PIV), capturing instantaneous flow fields with an extent of 12δ in the streamwise direction (*x*). In contrast to most studies to date, which have investigated the superstructures by analysing the large-scale *u*-fluctuations, here, we adopt a unique strategy to investigate the wall-normal (*w*) velocity fluctuations within the superstructure region. This is because deciphering smaller constituent *u*-motions from within a larger *u*-motion can be inconclusive, as can be noted from a sample direct numerical simulation (DNS) flow field shown in figure 2(*a*,*b*). On the other hand, the *w*-fluctuations can bring out the individual constituent motions more distinctly, which is evident from figure 2(*c*) and will be analysed here by computing conditional statistics. It can be noted from figure 2(*a*–*c*) that the individual *w*-eddies within the region associated with a long *u*-motion are much smaller in streamwise extent (than *u*), and exhibit sort of a clustered/packed organization plausibly leading to the appearance of a *u*-superstructure. This scenario is recreated in figure 2(*d*,*e*), using an idealized distribution of prograde vortices, which suggests the possibility of strong *u*- as well as *w*-correlations extending across large streamwise separations. Such a flow organization, which adds further credibility to the streamwise concatenation hypothesis, will be investigated here via conditional statistics from high Re_τ data. It is important to note that in the present study, any reference to concatenation henceforth refers to the spatial organization of constituent motions over extended streamwise distances, such as in figure 2(*d*,*e*). Given the experimental limitations, the study cannot directly comment on the dynamics/mechanism behind how this spatial organization comes into existence. Also, the terminology 'attached eddies' is used here to refer to any eddies/motions scaling with their distance from the wall, and hence is not limited to the eddies physically extending to the wall.

Measurement	Facility	Re_τ	ν/U_τ (in µm)	Δx^+	Δz^+	FOV ($x \times z$)	Reference
LFOV PIV	HRNBLWT	2500	42	26	26	$12\delta \times 1.2\delta$	de Silva *et al.* (2015, 2020)
LFOV PIV	HRNBLWT	5000	22	52	52	$12\delta \times 1.2\delta$	de Silva *et al.* (2015, 2020)
LFOV PIV	HRNBLWT	7500	15	75	75	$12\delta \times 1.2\delta$	de Silva *et al.* (2015, 2020)
PIV	HRNBLWT	14 500	24	37	37	$2\delta \times 0.4\delta$	de Silva *et al.* (2014)
Sonics	SLTEST	$O(10^6)$	78	1000	90	—	Hutchins *et al.* (2012)

Table 1. Table summarizing details of datasets comprising synchronized measurements of *u*- and *w*-fluctuations at various wall-normal locations; Re_τ for the various PIV datasets is based on δ estimated at the centre of the flow field (figure 3*a*). Terminology has been defined in § 2; Δx^+ and Δz^+ indicate viscous-scaled spatial resolution along *x* and *z* directions, respectively.

2. Experimental datasets and methodology

2.1. *Description of the experimental datasets*

Five multipoint datasets are used from previously published high Re_τ experiments (table 1). Four of these are acquired via two-dimensional (2-D) two-component PIV in the Melbourne wind tunnel (HRNBLWT; Marusic *et al.* 2015) and span the Re_τ range $\sim$ 2500–14 500. The test section of this wind tunnel has a cross-section of 0.92 m $\times$ 1.89 m, and has a large streamwise development length of $\sim$27 m, with maximum possible free-stream speeds (U_∞) of up to 45 ms^{-1}. Such a large-scale facility permits the generation of a sufficiently high Re_τ canonical boundary layer flow facilitated by substantial increment in its boundary layer thickness, along its long streamwise fetch. This capability is leveraged in the four PIV datasets employed in the present study, which will be described next.

Three of the PIV datasets comprise snapshots of very large streamwise wall-normal flow fields of a turbulent boundary layer ($x \times z \sim 12\delta \times 1.2\delta$), and are thus henceforth referred to as the LFOV PIV datasets (de Silva *et al.* 2015, 2020). To the best of the authors' knowledge, this is the only published laboratory-based dataset giving access to sufficient LFOV instantaneous flow fields at $Re_\tau \gtrsim 5000$ (to achieve statistical convergence), thereby making the analysis presented in this paper unique as well as ideally suited for investigating turbulent superstructures. The LFOV is made possible by stitching the imaged flow fields from eight high-resolution 14 bit PCO 4000 PIV cameras, each with a sensor resolution of 4008 $\times$ 2672 pixels. Figure 3(*a*) shows a schematic of the experimental set-up for the LFOV PIV, where the region shaded in orange indicates the individual FOVs combined from the eight cameras. These measurements were conducted at the upstream end of the test section, with the LFOV starting at $x \approx 4.5$ m from the start of the test section. The experiments were conducted at three free-stream speeds ($U_\infty \approx 10$, 20 and 30 ms^{-1}), which led to a corresponding variation in Re_τ of 2500, 5000 and 7500, respectively. Here, U_τ and δ used to estimate the flow Re_τ, were computed at the middle of the LFOV, using the method outlined in Chauhan, Monkewitz & Nagib (2009). The boundary layer thickness is nominally $\delta \approx 0.11$ m for all three Re_τ cases.

Considering the focus of the experiment was on a LFOV, a homogeneous seeding density was ensured across the entire test section of the tunnel for these measurements, and the particles were illuminated by a Big Sky Nd-YAG double pulse laser ($\sim$1 $\dot{m}$m thickness), delivering 120 mJ pulse^{-1}. The last optical mirror to direct this laser sheet was tactically placed within the test section (figure 3*a*), for ensuring adequate laser illumination levels across the LFOV. This optic arrangement, however, was sufficiently downstream of the PIV flow field and introduced no adverse effects (such as blockage, etc.) on the
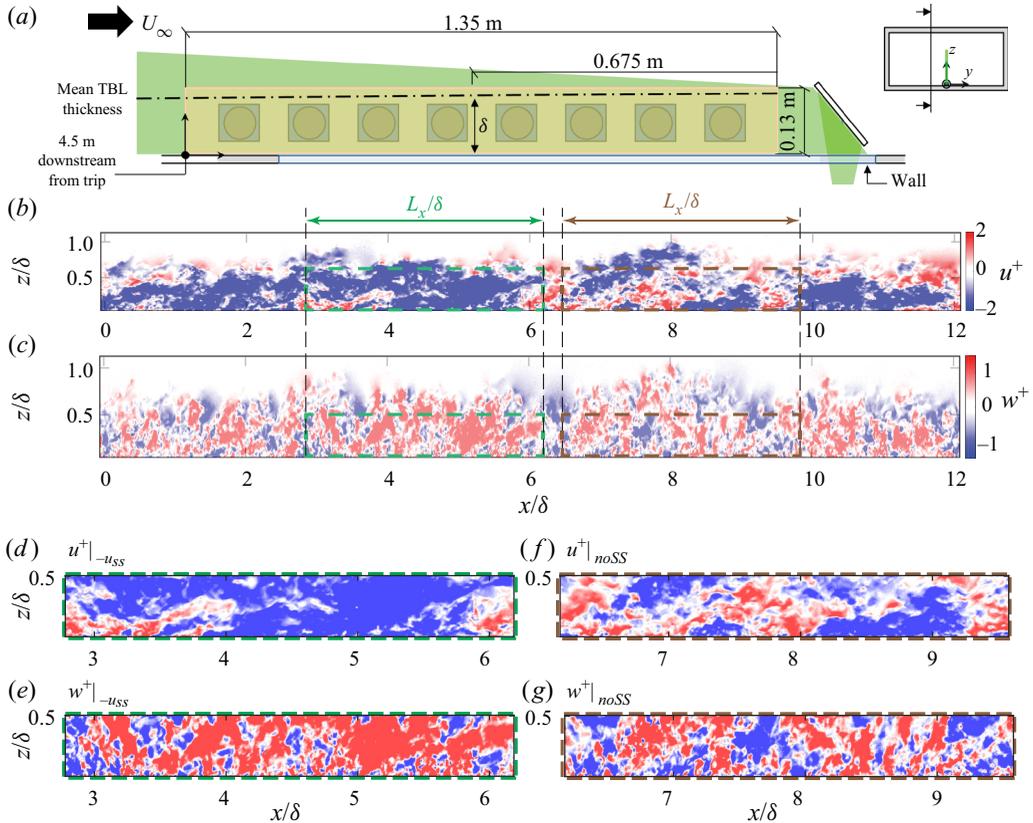
Figure 3. Schematic of the experimental set-up used to conduct LFOV PIV experiments in the streamwise wall-normal plane (*x*–*z*) in the HRNBLWT. Green shading indicates flow illuminated by the laser while the orange shading indicates the flow field cumulatively captured by the PIV cameras (shown in the background). Dash-dotted black line represents the streamwise evolution of the boundary layer thickness, with δ defined at the centre of the full flow field. (*b,c*) Instantaneous (*b*) u^+ and (*c*) w^+-fluctuations from the LFOV PIV dataset at $Re_\tau \approx 2500$. The dashed green box in (*b,c*) identifies a low-momentum turbulent superstructure ($-u_{ss}$) of length L_x based on the superstructure extraction algorithm described in § 2.2. (*d,e*) Show an expanded view of the *u*- and *w*-fluctuations within $-u_{ss}$, as identified in (*b,c*), respectively. Alternatively, the dashed brown box in (*b,c*) represents flow field of the same length×height as the dashed green box, but not associated with a turbulent superstructure (*noSS*). (*f,g*) Show an expanded view of the *u*- and *w*-fluctuations within the *noSS* region identified in (*b,c*), respectively.

measurement (de Silva *et al.* 2015). Figure 3(*b,c*) gives an example of the viscous-scaled *u*- and *w*-fluctuations estimated from the LFOV PIV experiment at $Re_\tau \approx 2500$, which successfully captures a turbulent superstructure (of length L_x), as highlighted by a dashed green box in the *u*-field. Analysis on such a dataset not only avoids uncertainties due to Taylor's hypothesis approximation (Dennis & Nickels 2008; del Álamo & Jiménez 2009; Wu *et al.* 2012), but also permits identification of these superstructures directly from an instantaneous flow field of a high Re_τ boundary layer (where superstructures are statistically significant). The latter represents another unique feature of the present study, and overcomes the limitations experienced by past experimental studies (Liu *et al.* 2001; Guala *et al.* 2006; Balakumar & Adrian 2007), which were restricted to isolating superstructure characteristics based on Fourier filtering, or proper orthogonal decomposition-based decomposition of ensemble/time-averaged statistics. The accuracy

of these LFOV PIV datasets have been firmly established in Appendix A, which compares the premultiplied 1-D spectra obtained from the present data with those acquired via multi-wire anemometry published previously (Morrill-Winter *et al.* 2015; Baidya *et al.* 2017). Readers can also refer to the same appendix section for details associated with the computation of the velocity spectra from PIV flow fields, which is relevant to the analysis presented ahead in the paper.

The fourth and final PIV dataset comprises relatively smaller flow fields in the *x–z* plane (in terms of δ-scaling), and is hence referred to as simply the PIV dataset. This was acquired at $U_\infty \approx 20$ ms^{-1}, close to the downstream end of test section ($x \approx 21$ m from the trip), where $\delta \approx 0.3$ m, yielding a high $Re_\tau \approx 14\,500$. The full velocity field captured in this experiment was also made possible by using the same eight PCO 4000 cameras, arranged in two vertical rows of four cameras each, to capture the significantly thicker boundary layer (refer to figures 1 and 2 of de Silva *et al.* 2014). This limits the streamwise extent of the flow field to $x \sim 2\delta$ in this case, and is hence not used for identifying the turbulent superstructures in instantaneous fields, but rather used to compute the two-point correlations of *u*- and *w*-fluctuations along the *z*-direction (limited to the inner region). It is owing to this reason that only a part of the full flow field ($x \times z \sim 2\delta \times 0.4\delta$), from this dataset, has been considered in the present study. The image pairs from all four PIV datasets were processed via an in-house PIV package developed by the Melbourne group (de Silva *et al.* 2014), with the final window sizes ($\Delta x^+, \Delta z^+$) used for processing given in table 1. Interested readers may refer to the cited references for further details about the experimental set-up and methodology adopted for acquiring these datasets.

The fifth dataset, which is at the highest $Re_\tau \sim O(10^6)$, was acquired at the Surface Layer Turbulence and Environmental Science Test (SLTEST) facility in the salt flats of western Utah. The data are acquired from a spanwise and wall-normal array of 18 sonic anemometers (Campbell Scientific CSAT3) arranged in an 'L'-shaped configuration (refer to figure 1 of Hutchins *et al.* 2012). While the full dataset comprises continuous measurements of all three velocity components as well as the temperature at the SLTEST site over a duration of nine days, here, we limit our attention solely to one hour of data associated with near-neutral (i.e. near canonical) atmospheric boundary layer conditions (Hutchins *et al.* 2012). These conditions were confirmed based on estimation of the Monin–Obukhov similarity parameter, determined on averaging across the 10 sonic anemometers placed along the spanwise array, at a fixed distance from the wall ($z \approx 2.14$ m). For the present analysis, we are solely interested in the *u*- and *w*-fluctuations measured synchronously by the nine sonic anemometers on the wall-normal array, which were placed in the range 1.42 m $\leq z \leq 25.69$ m with logarithmic spacing. Mean streamwise velocity measurements reported by Hutchins *et al.* (2012) confirm that all these *z*-locations fall within the log region of the atmospheric boundary layer. These data are also used here to compute the two-point correlations of *u*- and *w*-fluctuations along the *z*-direction, for comparison with those obtained from the PIV datasets acquired in the laboratory.

2.2. *Methodology employed to identify and extract turbulent superstructures*

In the present study, we are interested in computing conditional statistics of the velocity fluctuations associated with the superstructures, identified from the individual flow fields in the LFOV PIV dataset. To identify these structures, we need to first define what we mean by a superstructure, for which we draw inspiration from past studies that have investigated these motions based on 3-D instantaneous flow fields (Hutchins & Marusic 2007; Dennis

& Nickels 2011; Lee & Sung 2011). Those studies, as noted by Smits, McKeon & Marusic (2011), refer to superstructures as 'very long, meandering, features consisting of narrow regions of low-streamwise-momentum fluid flanked by regions of higher-momentum fluid', that 'have also been observed in the logarithmic and wake regions of wall flows'. Here, for the purpose of analysing 2-D velocity fields, we define superstructures as VLSMs that persist spatially with coherent regions of streamwise velocity, and account for a significant fraction of the streamwise turbulent kinetic energy. Identifying these structures from the PIV field, hence, requires establishing logical thresholds to the geometric and kinematic properties of the fluctuating u-field (Hwang & Sung 2018; de Silva *et al.* 2020). For this, we consider previous findings and adopt the following thresholds:

(i) $|u(x, z)| > \sqrt{\overline{u^2(z)}}$ (Liu *et al.* 2001), where $\sqrt{\overline{u^2(z)}}$ is the root-mean-square of the u-fluctuations at z;

(ii) streamwise extent, $L_x > 3\delta$ (Guala *et al.* 2006; Balakumar & Adrian 2007);

(iii) wall-normal extent should at least span across $2.6\sqrt{Re_\tau} \lesssim z^+ \lesssim 0.5Re_\tau$ (Guala *et al.* 2006; Balakumar & Adrian 2007; Hutchins & Marusic 2007; Deshpande *et al.* 2021*b*).

In the process of identifying a superstructure, the threshold associated with the streamwise turbulent kinetic energy (i.e. (i)) is considered first before applying thresholds associated with the geometric extent ((ii) and (iii)). With regards to criterion (ii), we acknowledge that past studies investigating 3-D instantaneous flow fields (Hutchins & Marusic 2007; Dennis & Nickels 2011; Lee & Sung 2011) have found superstructures to be as long as 10–20δ. However, statistical analysis based on 1-D one-/two-point correlations (Guala *et al.* 2006; Balakumar & Adrian 2007; Hutchins & Marusic 2007; Deshpande *et al.* 2021*b*) suggests these structures have relatively modest lengths (on average), in the range 3–6δ. Considering that the present analysis is also limited to 2-D flow fields, we adapt the estimates from past statistical analyses and consider u-structures with streamwise extent, $L_x > 3\delta$ as superstructures. Figure 3(*d*) gives an example of a $-u$ superstructure identified and extracted by the algorithm ($u|_{SS}$), based on the aforementioned thresholds from the full flow field depicted in figure 3(*b*) (highlighted by the dashed green box). Streamwise extent/length of the identified structures (L_x) is judged based on the length of a rectangular bounding box (along x) that fully encompasses the identified structure. Our superstructure identification algorithm extracts the rectangular 2-D flow field within this box to conduct further conditional analysis associated with the superstructures. Although the choice of a rectangular box inevitably also brings in some part of the flow not associated with a superstructure, it only forms a minor part ($\sim$20 %) of the bounding box, suggesting conditional statistics can be predominantly associated with the superstructures. Interested readers are referred to the supplementary material available at https://doi.org/10.1017/jfm. 2023.566, which provides a step-by-step description of the superstructure identification and extraction procedure from a 2-D PIV flow field.

Besides identifying a superstructure, which is indicated by a dashed green box in figure 3(*b,c*), the algorithm also identifies a region of same length × height as the green box but not associated with a superstructure ($u|_{noSS}$). The $u|_{noSS}$ flow field region is allocated by the algorithm in the same wall-normal range as $u|_{SS}$, but in a different streamwise location within the PIV image that does not satisfy criteria (i–ii) defined above, thereby ensuring it does not overlap with $u|_{SS}$. This practice of extracting $u|_{noSS}$, from the same PIV fields used to extract $u|_{SS}$ and of the same size as that of $u|_{SS}$, is conducted across all three LFOV datasets to form a set of $u|_{noSS}$ and $u|_{SS}$ of equal ensembles.
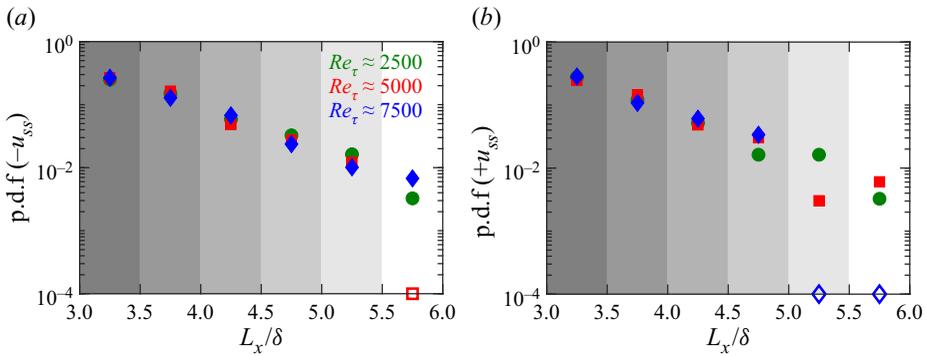
Figure 4. Probability density function (p.d.f.) of the lengths of the large and intense, (*a*) low and (*b*) high streamwise momentum motions detected by the superstructure extraction algorithm in PIV flow fields of various Re_τ. Background shading indicates the bin sizes used to estimate the p.d.f., for which the total number of detected superstructures (i.e. addition of $+u_{ss}$ and $-u_{ss}$) was used for normalization. Empty symbols indicate zero probability for the respective bin.

Conditional statistics are computed and compared from both $u|_{SS}$ and $u|_{noSS}$, with the latter considered to confirm that the trends depicted by the former are not an artefact of aliasing or insufficient ensembling/noise.

The superstructure extraction algorithm described above identified superstructures of both $+u$ and $-u$ signatures, of varying lengths, from the three LFOV PIV datasets. A summary of their streamwise extents is presented in the form of probability distribution function (p.d.f.) plots in figure 4. The plot is obtained by sorting the identified u-motions into bins of width 0.5δ (between $3.0 : 0.5 : 6.0$), based on their respective lengths (L_x). The population associated with each bin is then normalized by the total number of $-u$ and $+u$ superstructures identified by the algorithm (for $L_x > 3\delta$), which is then plotted in the figure. It can be noted from the plots that the p.d.f.s do not change significantly with Re_τ for structures of lengths, $L_x < 5\delta$. It is only when L_x is increased significantly ($> 5\delta$) that notable differences appear for different Re_τ. For example, no $-u$ or $+u$-structures are identified in certain PIV datasets while in others, the probability is low. Further, the logarithmic scaling of the vertical axis of the plots reveals that the population density decreases near exponentially as the criterion (ii) to identify a superstructure (i.e. minimum length, L_x) is increased. The effect of increasing the minimum streamwise extent of a u-structure to qualify as a superstructure, on the conditionally averaged statistics, has been documented in figure 15 in Appendix B. Given that an increase in L_x does not change the scaling behaviour, but significantly reduces the convergence of the conditioned statistics (due to fewer ensembles), reinforces the choice of $L_x \gtrsim 3\delta$ in criterion (ii) discussed above.

3. Mean statistics

Before investigating the conditionally averaged statistics associated with the super-structures, it is worth revisiting the scaling behaviour of the mean statistics, against which the former would be compared. Here, the mean statistics have been obtained by averaging across all 3000 flow fields, and considering the entire 12δ long flow fields in case of the LFOV PIV datasets. In the present study, since we are primarily interested in the w-velocity behaviour associated with superstructures, we investigate the mean spatial coherence of the w-carrying eddies in the log region of a high Re_τ boundary layer. We look at the spatial coherence in both the streamwise (figure 5) as well as wall-normal direction (figure 6), for
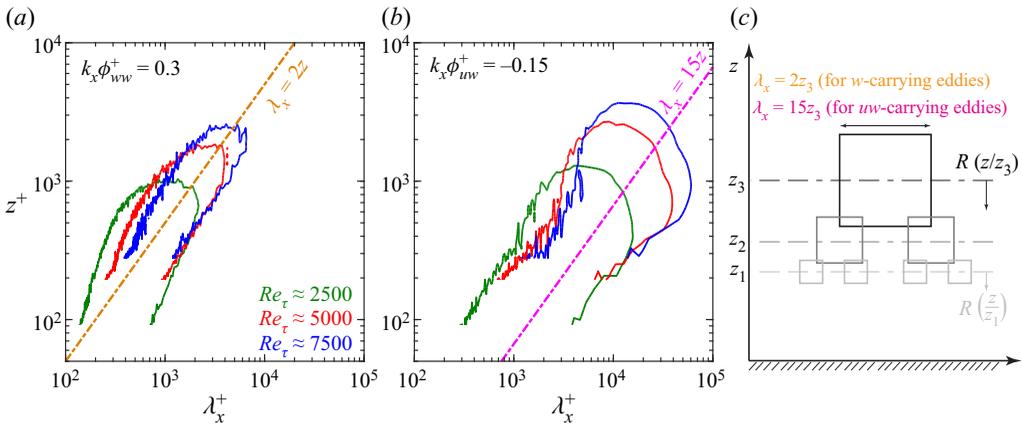
Figure 5. Iso-contours of the premultiplied streamwise 1-D (*a*) energy spectra of *w*-fluctuations and (*b*) co-spectra of the Reynolds shear stress plotted against z^+ and λ_x^+, computed from the LFOV PIV dataset at various Re_τ. Dash-dotted golden and magenta lines represent the relationships $\lambda_x \approx 2z$ and $\lambda_x \approx 15z$, respectively following Baidya *et al.* (2017). (*c*) Schematic of representative *w* and *uw*-carrying eddies centred at various distances from the wall (z_r) in the log region, with light to dark shading used to suggest an increase in z_r. Here, $R_{ww}(z/z_r)$ and $R_{uw}(z/z_r)$ respectively represent the vertical coherence of the *w*- and *uw*-carrying eddies centred at z_r.

both the *w*-fluctuations and the Reynolds shear stress (*uw*). Previous investigations on the vertical coherence have been rare compared with the streamwise coherence, particularly for the log region of a high Re_τ boundary layer, owing to the lack of large-scale PIV experiments of the kind utilized here. This makes the present investigation (figure 6) unique by itself.

Figures 5(*a*) and 5(*b*) depict the iso-contours of the premultiplied spectrogram of the *w*-velocity and the Reynolds shear stress, respectively, computed from the three LFOV PIV datasets. These are plotted as a function of λ_x^+ and z^+. The iso-contours for the *w*-velocity spectrograms can be seen centred around the linear (*z*-)scaling indicated by $\lambda_x = 2z$ for all Re_τ, which is consistent with previous observations in the literature (Baidya *et al.* 2017). Similarly, the iso-contours for the Reynolds shear stress spectrograms also follow a linear scaling ($\lambda_x = 15z$) for all Re_τ, again consistent with the literature (Baidya *et al.* 2017). This analysis not only validates the spectra estimated from the LFOV PIV, but also assists with the construction of a simplified 2-D conceptual picture of the *w*- and *uw*-carrying eddies in the log region of a high Re_τ boundary layer (figure 5*c*). Here, based on the *z*-scaling exhibited by the data, the lengths (λ_x) of the *w*- and *uw*-carrying eddies have been defined as $2z_r$ and $15z_r$, respectively, where z_r represents the distance of the eddy centre from the wall. This scaling confirms the association of these *w*- and *uw*-carrying eddies with Townsend's attached eddy hierarchy, according to which attached eddies scale with z_r (Townsend 1976; Baidya *et al.* 2017; Deshpande *et al.* 2021*a*).

While both these linear scalings, which represent the streamwise coherence of the *w*- and *uw*-carrying eddies, are well accepted in the literature, not much is known about the vertical/wall-normal coherence of the same eddying motions at high Re_τ. Several previous studies (Comte-Bellot 1963; Tritton 1967; Sabot, Renault & Comte-Bellot 1973; Hunt *et al.* 1987; Liu *et al.* 2001; Sillero, Jiménez & Moser 2014) have investigated their vertical coherence in low Re_τ canonical wall flows via traditional two-point correlations, providing interesting insights on their scaling. Here, we are inspired by one such interesting result reported in the seminal work of Hunt, Kaimal & Gaynor (1988), based on high Re_τ
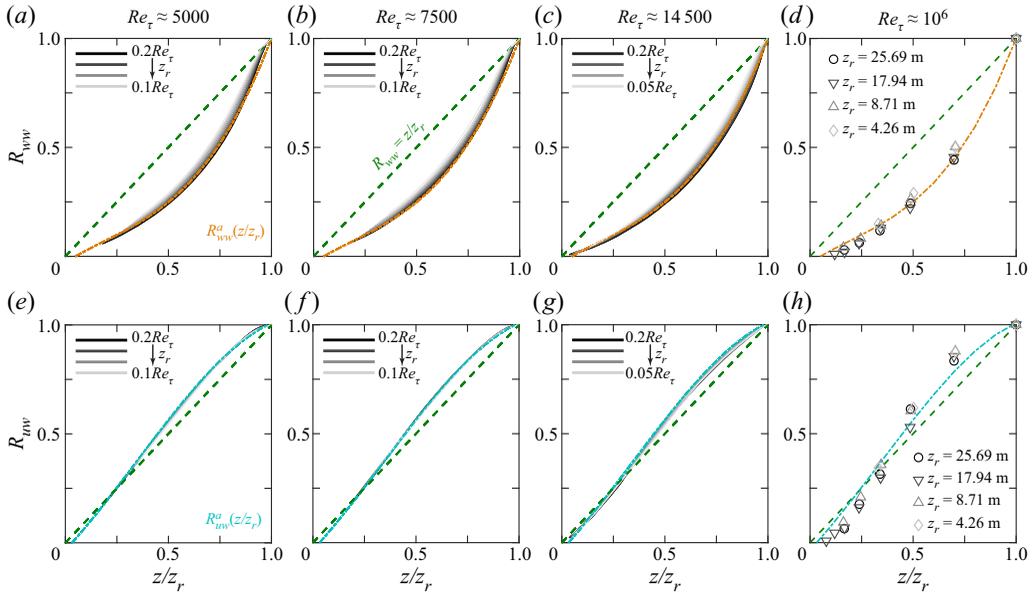
Figure 6. (*a–d*) Cross-correlation of *w*-fluctuations measured at z and z_r, normalized by $\overline{w^2}(z_r)$ for various z_r in the log region. (*e–h*) Cross-correlation between $u(z_r)$ and $w(z)$, normalized by $\overline{uw}(z_r)$ for the same z_r as in (*a–d*). Panels (*a,b,e,f*) are estimated from the LFOV PIV datasets while (*c,g*) have been computed from the PIV dataset. In case of the SLTEST dataset in (*d,h*), z_r listed in the legend corresponds to the 9th, 8th, 6th and 4th sonic positioned from the ground. Dashed green line corresponds to the linear relationship, z/z_r while dash-dotted golden and teal lines correspond to the least-squares fit R_{ww}^a and R_{uw}^a defined in (3.2), respectively.

unstably stratified atmospheric boundary layer data, who found the two-point correlation coefficients given by

$$R_{ww}\left(\frac{z}{z_r}\right) = \frac{\overline{w(z)w(z_r)}}{\overline{w^2}(z_r)} \quad \text{and} \quad R_{uw}\left(\frac{z}{z_r}\right) = \frac{\overline{w(z)u(z_r)}}{\overline{uw}(z_r)}, \qquad (3.1a,b)$$

to be a function of (z/z_r). Here, z_r acts as the reference wall-normal location fixed in the log region, thereby making R_{ww} (or R_{uw}) representative of the vertical coherence of the eddy centred at z_r. It should be noted here that these correlation functions are different from the conventionally used two-point correlations (which consider normalization by the root-mean-square of velocity at both z and z_r), and hence their values are not restricted between -1 and 1. Equations (3.1*a,b*), however, are ideally suited for the present study, which tests the self-similarity (i.e. z-scaling) of the vertical coherence of the momentum-carrying eddies. We compute these correlations for the four high Re_τ boundary layer datasets considered and plot them in figure 6, for various z_r restricted to the log region. It can be clearly observed that R_{uw} curves for varying z_r and Re_τ collapse over one another (represented by a line in teal colour based on least-squares fit), suggesting Re_τ-invariance via z-scaling of the vertical coherence of uw-carrying motions. On the other hand, the collapse in the R_{ww} curves is not as good for the relatively low Re_τ cases (<7500), but certainly gets better for the very high Re_τ atmospheric data (figure 6*d*). This case has a significantly thicker log region than the boundary layers generated in the laboratory, suggesting the influence of the wall behind the relatively poor collapse of R_{ww} at low Re_τ. Accordingly, the z-scaling of the R_{ww} curves has been represented by the golden lines in figure 6(*a–d*) (obtained by a least-squares fit), which are consistent with

969 A10-12

R_{ww} curves in figure 6(*d*), as well as R_{ww} estimated farthest from the wall ($z_r^+ \approx 0.2Re_\tau$) in figure 6(*a*–*c*). The analytical expressions associated with these golden and teal lines are

$$\left.\begin{aligned} R_{ww}^a\left(\frac{z}{z_r}\right) &= 1.007\left(\frac{z}{z_r}\right)^3 - 0.56\left(\frac{z}{z_r}\right)^2 + 0.58\left(\frac{z}{z_r}\right) - 0.027, \quad \text{and} \\ R_{uw}^a\left(\frac{z}{z_r}\right) &= -0.65\left(\frac{z}{z_r}\right)^3 + 0.65\left(\frac{z}{z_r}\right)^2 + 1.03\left(\frac{z}{z_r}\right) - 0.03. \end{aligned}\right\} \tag{3.2}$$

The fact that R_{ww} and R_{uw} are solely a function of z/z_r represents geometric self-similarity in the vertical coherence of the w- and uw-carrying inertial eddies, reaffirming their association with Townsend's attached eddies. The analytical forms in (3.2) can thus be used in data-driven coherent structure-based models (Deshpande *et al.* 2021*b*) to simulate high Re_τ boundary layers (such as atmospheric surface layers). It is worth noting that the collapse in the R_{uw} and R_{ww} curves, observed in figure 6, does not exist for w- and uw-carrying eddies centred far outside the log region of the boundary layer (i.e. $z_r > 0.2\delta$; not shown here), which may be due to the growing influence of the turbulent/non-turbulent interface in the outer region (de Silva *et al.* 2014). Investigations for z_r below the log region, however, were not possible owing to insufficient data points captured by the LFOV PIV.

4. Conditionally averaged statistics associated with superstructures

With the scaling behaviour of the mean statistics established in §3, we progress next towards analysing the conditionally averaged statistics (spectra and correlations) associated with superstructures. Figure 7 plots the conditionally averaged, premultiplied u-spectra computed from the extracted flow fields associated with superstructures (figure 3*d*), from the three LFOV PIV datasets. The spectra are plotted for $z^+ \approx 2.6\sqrt{Re_\tau}$ and $0.5Re_\tau$, and estimated individually from the extracted flow fields associated with low-momentum ($k_x\phi_{uu}^+|_{-u_{ss}}$; in blue) and high-momentum superstructures ($k_x\phi_{uu}^+|_{+u_{ss}}$; in red). Also plotted is the conditionally averaged spectrum considering both $-u_{ss}$ and $+u_{ss}$ ($k_x\phi_{uu}^+|_{-u_{ss},+u_{ss}}$; in green), which is compared against the mean u-spectra shown in figure 14(*a*–*c*). A noteworthy observation from the conditionally averaged spectra ($k_x\phi_{uu}^+|_{-u_{ss},+u_{ss}}$) is the enhanced large-scale energy ($\lambda_x^+ \gtrsim 10^4$) seen for all three Re_τ cases. These enhanced energy levels are due to the significant streamwise turbulent kinetic energy associated with the superstructures, which is captured in the extracted flow fields and averaged across fewer ensembles, than those used for obtaining the mean spectra.

To confirm that these trends are not an artefact of aliasing or ensembling, figure 8 compares the conditionally averaged spectra associated with superstructures (green boxes in figure 3*c*) with that not associated with the superstructures (brown boxes in figure 3*c*). Given that both the conditional spectra are estimated from the same number of extracted flow fields, of the same length × height, the enhanced energy in the largest scales for $k_x\phi_{uu}^+|_{-u_{ss},+u_{ss}}$ (compared with $k_x\phi_{uu}^+|_{noSS}$) can be unambiguously associated with the turbulent superstructures. These trends give us confidence regarding the efficacy of the superstructure extraction algorithm. Also, they indicate that the scalings observed from the conditionally averaged u-, w-statistics can be associated with the constituent motions of superstructures. This is one of the advantages of analysing VLSMs based on extraction of instantaneous flow fields (present study), as compared with the much simpler approach of Fourier filtering (past studies).

Another interesting observation from the conditional spectra for low- and high-momentum motions, $k_x\phi_{uu}^+|_{-u_{ss}}$ and $k_x\phi_{uu}^+|_{+u_{ss}}$, is their starkly different behaviour
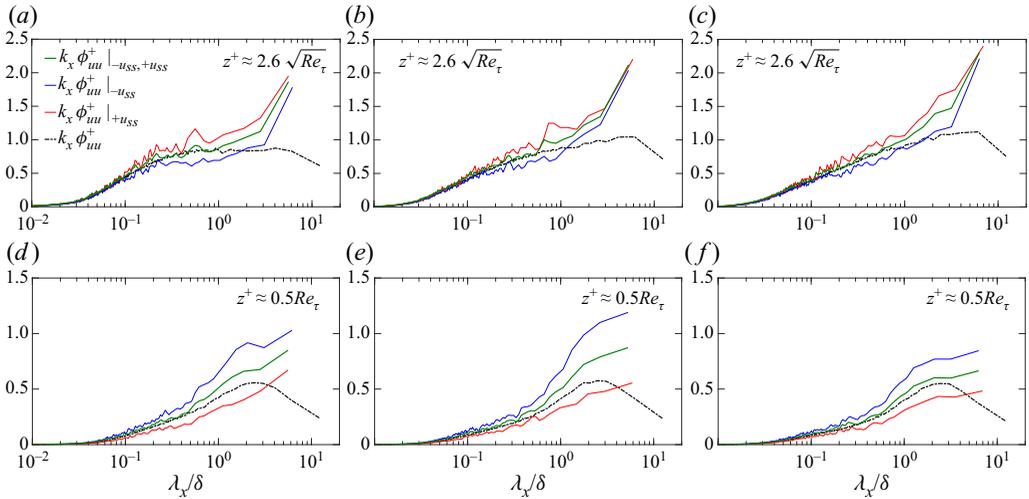
Figure 7. (a–f) Premultiplied 1-D spectra of the u-fluctuations plotted vs λ_x/δ at (a–c) $z^+ \approx 2.6\sqrt{Re_\tau}$ and (d–f) $z^+ \approx 0.5Re_\tau$ for LFOV PIV data at $Re_\tau \approx$ (a, d) 2500, (b,e) 5000 and (c,f) 7500. Dashed black lines correspond to the mean spectra obtained by ensembling across 3000 PIV images of the full flow field. While, the solid blue and red lines represent conditional spectra computed from the u-flow field extracted based on identification of a $-u_{ss}$ and $+u_{ss}$, respectively. The spectrum in green is computed by ensembling across both $-u_{ss}$ and $+u_{ss}$.
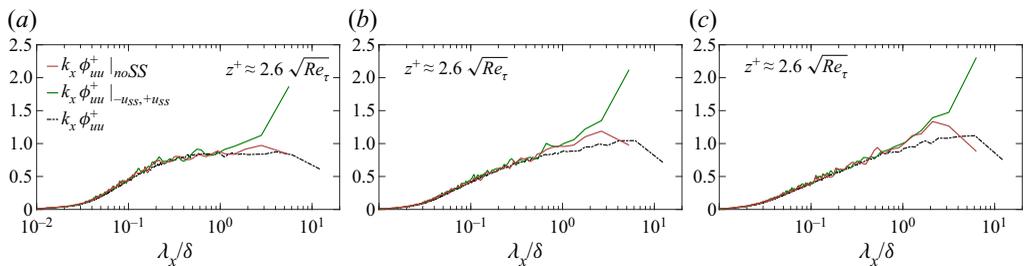
Figure 8. Premultiplied 1-D spectra of the u-fluctuations plotted vs λ_x/δ at $z^+ \approx 2.6\sqrt{Re_\tau}$ for $Re_\tau \approx$ (a) 2500, (b) 5000 and (c) 7500. The mean spectrum estimated from the full flow field (in black lines) is ensembled across all 3000 fields. While, the conditional spectrum corresponds to extracted flow fields ($\sim$300) of the same length $\times$ height associated (in green) and not associated (in brown) with the superstructures.

in the lower portion of the log region (figure 7a–c) and outside of it (figure 7d–f). While $k_x\phi^+_{uu}|_{+u_{ss}} > k_x\phi^+_{uu}|_{-u_{ss}}$ for $z^+ \approx 2.6\sqrt{Re_\tau}$, it is *vice versa* for $z^+ \approx 0.5Re_\tau$, which is in accordance with previous observations made by Hutchins & Marusic (2007). The study reported that the turbulent structures associated with $+u_{ss}$ are more energetic than those associated with $-u_{ss}$, in the lower part of the log region. This behaviour, however, is reversed in the upper part of the log region and beyond, which is consistent with our observations from figure 7, reaffirming confidence in the extracted flow fields.

With the efficacy of the superstructure extraction algorithm now established, we shift our focus to the statistical quantity of primary interest: conditionally averaged, premultiplied w-spectra associated with superstructures. Figure 9(a–f) plots $k_x\phi^+_{ww}|_{-u_{ss}}$, $k_x\phi^+_{ww}|_{+u_{ss}}$ and $k_x\phi^+_{ww}|_{-u_{ss},+u_{ss}}$ for $z^+ \approx 2.6\sqrt{Re_\tau}$ and $0.5Re_\tau$ computed from all three LFOV PIV datasets. Here again, $k_x\phi^+_{ww}|_{+u_{ss}} > k_x\phi^+_{ww}|_{-u_{ss}}$ for $z^+ \approx 2.6\sqrt{Re_\tau}$, and
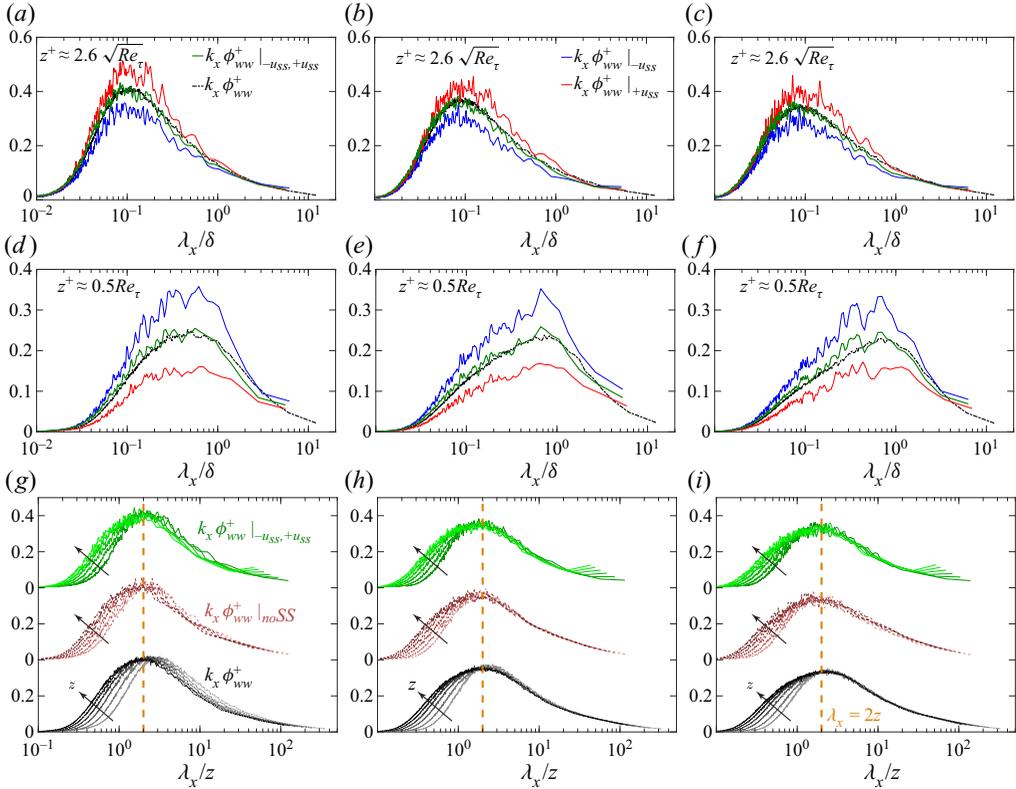
969 A10-14

Figure 9. (*a–f*) Premultiplied 1-D spectra of the *w*-fluctuations plotted vs λ_x/δ at (*a–c*) $z^+ \approx 2.6\sqrt{Re_\tau}$ and (*d–f*) $z^+ \approx 0.5Re_\tau$ for large FOV PIV data at $Re_\tau \approx$ (*a, d, g*) 2500, (*b,e,h*) 5000 and (*c,f,i*) 7500. Dashed black lines correspond to the mean spectra obtained by ensembling across 3000 PIV images of the full flow field while the solid blue and red lines represent conditional spectra computed from the extracted *w*-flow fields associated with $-u_{ss}$ and $+u_{ss}$, respectively. The spectrum in green corresponds to all extracted *w*-flow fields, associated with both $-u_{ss}$ and $+u_{ss}$. (*g–i*) Premultiplied 1-D spectra of *w*-velocity plotted vs λ_x/z at various z^+ within the log region ($2.6\sqrt{Re_\tau} \lesssim z^+ \lesssim 0.15Re_\tau$). Colour coding is the same as that defined for plots (*a–f*). Line plots in brown correspond to conditional spectra $k_x\phi^+_{ww}|_{noSS}$ computed from extracted flow fields of the same length $\times$ height as the $k_x\phi^+_{ww}|_{-u_{ss},+u_{ss}}$, but not associated with the superstructures. Dashed golden lines represent the linear scaling, $\lambda_x = 2z$.

vice versa for $z^+ \approx 0.5Re_\tau$, which is consistent with the behaviour noted for the *u*-spectra in figure 7. Interestingly $k_x\phi^+_{ww}|_{-u_{ss},+u_{ss}}$, which represents *w*-energy associated with both $-u_{ss}$ and $+u_{ss}$, can be seen to be overlapping with the mean *w*-spectra, for both z^+ and all three Re_τ considered in figure 9 (except at the largest λ^+_x). This suggests that the *w*-carrying eddies within the superstructures conform to the inertia-dominated *z*-scaled eddies predominant in the log region (figure 5). To test the *z*-scaling characteristics of $k_x\phi^+_{ww}|_{-u_{ss},+u_{ss}}$, we plot it for various z^+ corresponding to the log region in figure 9(*g–i*). Remarkably, $k_x\phi^+_{ww}|_{-u_{ss},+u_{ss}}$ exhibits *z*-scaling behaviour similar to the mean spectra for $\lambda_x \gtrsim 2z$, across all three Re_τ, suggesting that the geometrically self-similar attached eddies are likely the constituent motions of the superstructures. Further, the peak of $k_x\phi^+_{ww}|_{-u_{ss},+u_{ss}}$ also scales with $\lambda_x = 2z$, which is consistent with the mean spectra.

A unique observation associated with $k_x\phi^+_{ww}|_{-u_{ss},+u_{ss}}$, as compared with other spectra plotted in figure 9, is the slightly enhanced energy at the very large λ_x. There are two possible interpretations to this very-large-scale peak, with the first (and the most likely
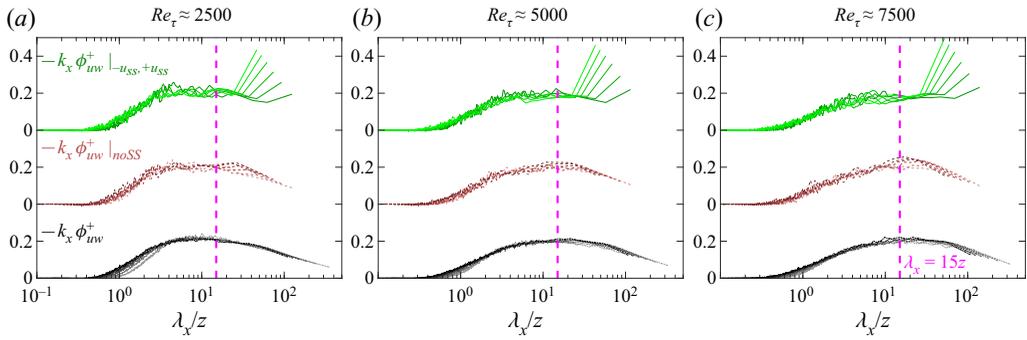
Figure 10. (*a–c*) Premultiplied 1-D co-spectra of the Reynolds shear stress plotted vs λ_x/z at various z^+ within the log region ($2.6\sqrt{Re_\tau} \lesssim z^+ \lesssim 0.15Re_\tau$). Dashed black lines correspond to the mean spectra obtained by ensembling across 3000 PIV images of the full flow field. The spectra in green correspond to all extracted u, w-flow fields, associated with both $-u_{ss}$ and $+u_{ss}$. Line plots in brown correspond to conditional spectra $k_x\phi_{uw}^+|_{noSS}$ computed from extracted flow fields of the same length × height as the $k_x\phi_{uw}^+|_{-u_{ss},+u_{ss}}$, but not associated with the superstructures. Dashed magenta lines represent the linear scaling, $\lambda_x = 15z$.

one) associated with the preservation of the covariance tensor (i.e. $\overline{uw}$) for the large scales. Based on the definition of the structure parameter, which is essentially the normalized form of $\overline{uw}$ that tends to $\sim O(1)$ for the large scales, conditioning the *w*-field based on a large-scale *u*-structure is bound to yield non-zero *w*-energy in the large scales, as a mathematical artefact. The other possible interpretation is the presence of a physically long *w*-eddy in the flow field, on conditioning of the flow based on a turbulent superstructure. Considering the instantaneous *w*-field discussed previously in figure 2(*c,e*), however, the second scenario seems very less likely, and this is reaffirmed via further analysis in § 4.1. The fact that the very-large-scale peak is not an artefact of aliasing or experimental noise is confirmed by considering $k_x\phi_{ww}^+|_{noSS}$ plotted for the same z^+-range in figure 9(*g–i*). Since $k_x\phi_{ww}^+|_{noSS}$ is estimated based on the same number of ensembles and length × height of the extracted flow fields as $k_x\phi_{ww}^+|_{-u_{ss},+u_{ss}}$, the former would have also had enhanced energy levels at large λ_x^+, if these peaks were owing to aliasing or noise.

Another way to reaffirm the close association between the geometrically self-similar attached eddies and the superstructures is by analysing the Reynolds shear stress. Previous studies (Liu *et al.* 2001; Guala *et al.* 2006; Balakumar & Adrian 2007) have found superstructures to carry a significant proportion of the Reynolds shear stress in the log region, and this is confirmed by the comparison of the Reynolds shear stress co-spectra presented in figure 10 at various Re_τ. This figure plots the conditionally averaged co-spectra associated with the superstructures ($k_x\phi_{uw}^+|_{-u_{ss},+u_{ss}}$), the co-spectra not associated with the superstructures ($k_x\phi_{uw}^+|_{noSS}$), as well as the ensemble-averaged co-spectra ($k_x\phi_{uw}^+$) at various z^+ within the log region. Similar to that noted for the *w*-spectra, the *z*-scaling observed in the ensemble-averaged co-spectra ($\lambda_x = 15z$; figure 5*b*) is also noted for $k_x\phi_{uw}^+|_{-u_{ss},+u_{ss}}$, confirming our claim that the self-similar motions coexist within the superstructure region. This comparison between $k_x\phi_{uw}^+|_{-u_{ss},+u_{ss}}$ and $k_x\phi_{uw}^+$ also showcases the significance of analysing the VLSMs by extracting instantaneous flow fields, than by using pure Fourier filtering. While the latter is simpler to execute, it does not present the 'full physical picture' associated with the very-large-scale motions. It is only after extraction of the instantaneous flow fields at high Re_τ that the present study can confirm the *z*-scaling characteristics associated with the constituent motions of the superstructures ($k_x\phi_{uw}^+|_{-u_{ss},+u_{ss}}$). In figure 10, again, high energy levels can
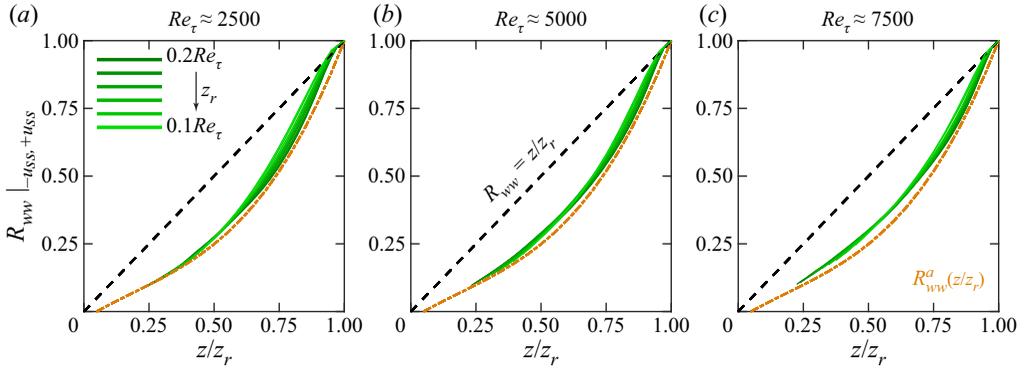
969 A10-16

Figure 11. (a–f) Conditionally averaged correlations between w-fluctuations at z and z_r, normalized by $\overline{w^2}(z_r)$ for various z_r. The correlations have been computed from the extracted w-flow fields associated with both $-u_{ss}$ and $+u_{ss}$. Dashed black line corresponds to the linear relationship, z/z_r while dashed dotted golden line corresponds to R_{ww}^a defined in (3.2).

be noted in $k_x\phi_{uw}^+|_{-u_{ss},+u_{ss}}$ at very large λ_x, the magnitude of which is much greater than the energy levels for $k_x\phi_{uw}^+|_{noSS}$ and $k_x\phi_{uw}^+$ at the same λ_x. Further analysis is presented in § 4.1 to reaffirm that these peaks do not represent very-large-scale w-motions existing in the physical flow field.

While the conditional 1-D spectra brings out the geometric characteristics of the constituent motions along the streamwise direction, their characteristics along the wall-normal direction can be understood by computing the two-point correlations (R_{ww}; (3.1a,b)) for the extracted flow fields. Figure 11 plots $R_{ww}|_{-u_{ss},+u_{ss}}$, i.e. the two-point correlations computed from the w-fluctuations associated with both $-u_{ss}$ and $+u_{ss}$, for z_r limited to the log region. These are estimated for all three LFOV PIV datasets and compared with the least-squares fit (given by (3.2)) estimated from the mean statistics (plotted with a golden line). Consistent with our observations based on the mean statistics in figure 6, the collapse in the $R_{ww}|_{-u_{ss},+u_{ss}}$ curves is not very good at low Re_τ but improves significantly at $Re_\tau \approx 7500$. Interestingly, however, $R_{ww}|_{-u_{ss},+u_{ss}}$ curves estimated at all Re_τ are close to the empirically obtained least-squares fit. Hence, investigation of the vertical coherence of the w-carrying eddies (associated with superstructures) also indicates that the geometrically self-similar eddies coexist within superstructure region, in line with interpretations based on figures 9 and 10. While the present study lacks the analysis to investigate the spanwise coherence of the constituent motions, consideration of the present findings in light of the recent knowledge on the log region (Hwang & Sung 2018; Deshpande *et al.* 2020, 2021a,b) suggests that they would likely exhibit self-similar characteristics along the span as well. Notably, Deshpande *et al.* (2020, 2021b) found that the spanwise extent of the wall-coherent, intermediate-scaled motions ($\lambda_x \lesssim 4\delta$) varies self-similarly with respect to their streamwise extent, which directly corresponds to the scale range associated with the constituent motions of the superstructures.

4.1. *Physical interpretations and discussions on the conditionally averaged statistics*

Here, we discuss the physical interpretation of the conditionally averaged spectra presented in figures 7–10, and how it advances our understanding of the constituent motions forming the turbulent superstructures. Given the geometry of individual w-eddies does not physically conform with the very-large-scale peaks noted in $k_x\phi_{ww}^+|_{-u_{ss},+u_{ss}}$ and

$k_x\phi_{uw}^+|_{-u_{ss},+u_{ss}}$ (discussed previously based on figure 2*c*,*e*), these peaks are likely an artefact of the preservation of the covariance tensor, which is a property of the Fourier transform. However, the non-zero correlation between *u* and *w*-fluctuations, at large λ_x, has often been misinterpreted to be representative of instantaneous *w*-features physically as long as the superstructures (as also highlighted by Lozano-Durán *et al.* 2012; Sillero *et al.* 2014), especially when one analyses it from the perspective of the structure parameter ($\sim O(1)$ for large λ_x). Here, we prove from our analysis that this interpretation is incorrect. If one observes $w|_{ss}$ plotted in figure 3(*e*), which is conditioned with respect to a $-u$ superstructure, it is clear there are no long and energetic *w*-features extending beyond 3δ. To the best of the authors' knowledge, energetic *w*-features of such long streamwise extents have never been noted in instantaneous flow fields, and their absence can also be confirmed from the negligible energy in the 1-D *w*-spectra plotted in figure 5(*a*), or in the literature (Baidya *et al.* 2017). Absence of very long ($\gtrsim 3\delta$) *w*-features also means there are no very-large-scale Reynolds shear stress-carrying motions in the instantaneous flow (Lozano-Durán *et al.* 2012; Sillero *et al.* 2014). Such misinterpretations are the source for the long-standing contradictions between the attached eddy hypothesis and past studies (Guala *et al.* 2006; Balakumar & Adrian 2007; Wu *et al.* 2012) investigating the Reynolds shear stress co-spectra (refer § 1), which we attempt to clarify here.

To reaffirm that the very-large-scale peaks in $k_x\phi_{ww}^+|_{-u_{ss},+u_{ss}}$ do not correspond with very long and energetic *w*-features in the instantaneous flow, figure 12 analyses the streamwise extent of *w*-eddies (L_x^w) in the extracted $w|_{SS}$ and $w|_{noSS}$ fields. For this analysis, the same algorithm is deployed to identify and characterize the *w*-eddies, as used to identify and extract superstructures in the *u*-field (refer § 2.2 and the supplementary material). Figure 12(*a*,*b*) represents the same $w|_{SS}$ and $w|_{noSS}$ fields as in figure 3(*e*,*g*),

but only consider motions with strong fluctuations (i.e. $|w_{SS}|, |w_{noSS}| > 1.3\sqrt{\overline{w^2}(z)}$). This threshold is based on Dennis & Nickels (2011) and assists with identification and extraction of individual, energetic *w*-eddies. Figure 12(*c*,*d*) presents the probability distribution functions (p.d.f.) of the streamwise extents of the *w*-eddies identified within $w|_{SS}$ and $w|_{noSS}$ flow fields, extracted across all three PIV datasets. The plots confirm that the streamwise extent of *w*-eddies is limited to $\lesssim 3\delta$ across both $w|_{SS}$ and $w|_{noSS}$. This wavelength range closely corresponds with the geometrically self-similar hierarchy of eddies exhibiting distance-from-the-wall scaling in figure 9, reaffirming the key finding of this study, based on direct analysis of the physical flow field. Although not shown here, a similar analysis on the Reynolds shear stress-carrying eddies also yields the same conclusion, reinforcing our earlier statements on the interpretation of $k_x\phi_{uw}^+|_{-u_{ss},+u_{ss}}$. The analysis also confirms that energetic *w*-eddies do not physically extend along *x*, as long as the superstructures ($> 3\delta$), meaning the only possible way of observing a physically long *w*-feature is when the individual *w*-eddies align along the *x*-direction. Indeed, the $w|_{SS}$ flow field indicates a much more closely packed/clustered organization of the individual *w*-eddies, compared with $w|_{noSS}$, in the *x*-direction (figure 12*a*,*b*). However, since the present analysis uses snapshot 2-D PIV data, this study cannot definitively comment on the dynamics behind the formation of superstructures. But, the conditional analysis presented in this section does lend empirical support in favour of the formation of superstructures via streamwise concatenation of the intermediate-scaled eddies (Adrian *et al.* 2000). Interested readers are referred to the supplementary material, where we have utilized a simplified coherent structure-based model (i.e. the attached eddy model), to demonstrate a statistically plausible scenario of self-similar eddies aligning in *x* to 'form' a superstructure.
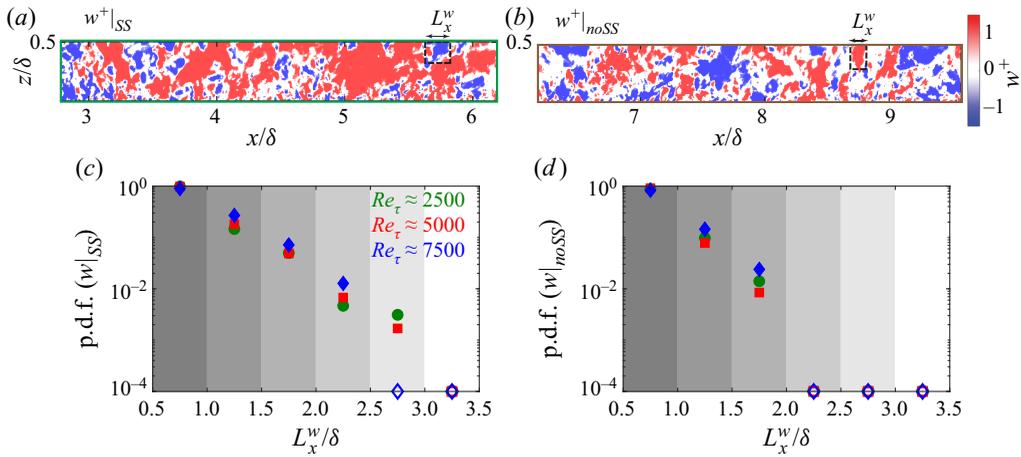
Figure 12. (*a,b*) Examples of intense *w*-fluctuations ($|w_{SS}|, |w_{noSS}| > 1.3\sqrt{\overline{w^2}(z)}$) present within flow fields associated (*a*) with superstructures ($w|_{SS}$) and (*b*) not associated with superstructures ($w|_{noSS}$). The $w|_{SS}$ and $w|_{noSS}$ flow fields used as examples in (*a,b*) essentially correspond to the extracted fields shown in figure 3(*e,g*). (*c,d*) Probability density function (p.d.f.) of the lengths (L_x^w) of intense (*c*) $w|_{SS}$ and (*d*) $w|_{noSS}$ motions extracted from the corresponding flow fields at various Re_τ. Background shading indicates the bin size used to estimate the p.d.f., for which the total number of detected $w|_{SS}$ and $w|_{noSS}$ were used for normalization. Empty symbols indicate zero probability for the respective bin.

The present results are also consistent with the conclusions of Lozano-Durán *et al.* (2012), who found large-scale Reynolds shear stress-carrying structures to be essentially a concatenation of smaller *uw*-carrying eddies, having lengths ∼3 times their height. This also clarifies the contradiction in the literature on the 'active'/'inactive' status of the very-large-scale *u*-motions (i.e. superstructures). Given there are no very-large-scale *w*- (and consequently *uw*-) features in the instantaneous flow, the superstructures are indeed inactive as per the definition of Townsend (Deshpande *et al.* 2021*a*). Present evidence indicates that the superstructures comprise several *z*-scaled *w*-carrying (i.e. active) motions, which explains the past empirical observations of superstructures carrying significant Reynolds shear stress.

5. Concluding remarks

The present study analyses large-scale PIV datasets, acquired in moderate to high Re_τ turbulent boundary layers ($2500 \lesssim Re_\tau \lesssim 7500$), to investigate the constituent motions of the turbulent superstructures. Considering that superstructures are statistically significant only at $Re_\tau \gtrsim 2000$ (Hutchins & Marusic 2007), the present datasets (providing sufficient scale separation) are ideally suited to identifying superstructures and analysing their constituent motions. These unique datasets accurately capture the inertia-dominated instantaneous *u*- and *w*-fluctuations across a large streamwise wall-normal plane, extending up to 12δ in the *x*-direction. This facilitates a comprehensive investigation of the horizontal (via 1-D spectra) as well as vertical coherence (via two-point correlations) of the Reynolds shear stress-carrying eddies coexisting in the log region, which are responsible for the momentum transfer in a high Re_τ boundary layer (Baidya *et al.* 2017; Deshpande *et al.* 2021*a*). The statistics bring out the geometric self-similarity of these energetically significant eddies, which complements the well-established knowledge on the self-similarity exhibited by the wall-parallel velocity components in a canonical
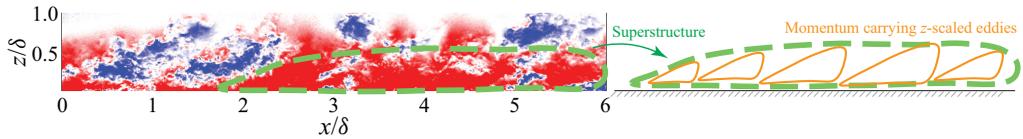
Figure 13. Conceptual representation of the main conclusion of this study: z-scaled eddies are likely the constituent motions forming the turbulent superstructures.

flow (Baars *et al.* 2017; Hwang & Sung 2018; Deshpande *et al.* 2020). We note that this motivates undertaking similar investigations of the momentum and heat flux in thermally stratified wall-bounded flows at high Re_τ (for example atmospheric boundary layers), which can likely assist with coherent structure-based modelling of these practically relevant flows.

The empirically derived scaling behaviour observed from these mean statistics (spectra and correlations) provide a benchmark for comparing and contrasting with the conditionally averaged statistics, associated with the turbulent superstructures. Such conditional statistics are made possible by the large-scale PIV flow fields, which permit identification of the superstructures directly from instantaneous flow fields. These statistics present a comprehensive picture of the superstructures, in comparison with the limited information available based on modal decompositions, used often in past studies (such as Fourier filtering, etc.). Considering the ambiguity involved while interpreting the smaller constituent motions from a u-flow field, the present study adopts the approach of investigating the w-fluctuations within the superstructure region, to understand its constituent motions. Notably, the conditional streamwise w- and uw-spectra exhibit the classical z-scaling ($\lambda_x = 2z$; $\lambda_x = 15z$) in the intermediate scale range (Baidya *et al.* 2017), clearly suggesting that geometrically self-similar eddies co-exist within the superstructure region (represented schematically in figure 13). The same conclusion is demonstrated through the conditional two-point w-correlations, along the vertical direction, which also exhibit self-similar scaling similar to that noted for the mean flow. Investigations of these kinds are only possible on analysing instantaneous flow fields, highlighting the uniqueness of the present large-scale high Re_τ PIV dataset.

The argument regarding the self-similar motions, as the likely constituent motions of the turbulent superstructures, is reaffirmed by analysing the geometry and population of individual w-eddies associated with these very-large-scaled structures. The maximum streamwise extent of the energetic w-eddies was found limited to $\lesssim 3\delta$ within the superstructures, similar to that noted outside a superstructure, and conforming to the self-similar hierarchy of scales. The same analysis also revealed the spatial organization of these constituent w-eddies within the superstructures, which is consistent with the streamwise concatenation argument of forming superstructures. This also helps clarify longstanding contradiction in the literature on the active/inactive behaviour of the superstructures (Guala *et al.* 2006; Balakumar & Adrian 2007; Wu *et al.* 2012). Since there are no very-large-scale w- and uw-features in the instantaneous flow, the superstructures are indeed inactive per the definition of Townsend (Deshpande *et al.* 2021*a*). However, the study finds that superstructures comprise several z-scaled Reynolds shear stress-carrying (i.e. active) motions (Lozano-Durán *et al.* 2012), which explains the past empirical observations of these very-large-scaled motions carrying significant Reynolds shear stress.

The present study concludes that superstructures are an assemblage of the attached eddy hierarchy in the streamwise wall-normal plane, hinting at a well-defined spatial organization of the attached eddies. This contradicts the original hypothesis of Townsend

(1976), per which attached eddies are randomly distributed in the flow domain, suggesting the need to revisit the hypothesis (this has also been tested based on synthetic flow fields and presented in the supplementary material). The present empirical findings, specifically the Re_τ-invariance of the vertical coherence of inertial eddies (R_{ww}, R_{uw}), can also be used to further improve coherent structure-based models, such as the attached eddy model (Marusic & Monty 2019). This is possible through extending the data-driven approach proposed recently in Deshpande *et al.* (2021*b*), by defining the geometry of the representative eddies based on the least-squares fits presented in (3.2). The present findings would also benefit the attached eddy model by acting as empirical evidence, to model superstructures as clusters of self-similar (attached) eddies, organized along the streamwise direction.

Author ORCIDs.

Ⓑ Rahul Deshpande https://orcid.org/0000-0003-2777-2919;

Ⓑ Charitha M. de Silva https://orcid.org/0000-0001-9517-4318;

Ⓑ Ivan Marusic https://orcid.org/0000-0003-2700-8435.

Appendix A. Comparisons of energy spectra obtained from LFOV PIV with published hot-wire data

Figure 14 plots the premultiplied streamwise 1-D spectra of the streamwise and wall-normal velocity components, as well as the Reynolds shear stress obtained from the LFOV PIV dataset. Throughout this study, we are limited to studying the 1-D velocity spectrum, which is a function of the streamwise wavelengths, λ_x and distance from the wall, z. The spectrum at z is computed by first extracting the velocity fluctuations measured at various streamwise locations at the given height, from a PIV flow field. The extracted 1-D array is zero padded with sufficient elements to avoid uncertainties due to a 'tight' box size. Then, a Hamming window function (Bendat & Piersol 2011) is considered to reduce spectral leakage, which is non-zero for the length/array size of the original PIV flow field (along x) and zero outside (to correspond with the zero padding). Next, the array associated with the Hamming window function is multiplied on an element-by-element basis with the zero-padded 1-D array, comprising the velocity fluctuations. Fourier transform is then computed on this 1-D array to get the streamwise 1-D spectrum of the velocity component. This procedure was adopted while computing each spectrum (ensemble-averaged as well as the conditionally averaged spectra) presented in this study. While the Hamming window was used predominantly in this study, this spectrum was also compared with spectra computed using Dirichlet or Welch window functions (Bendat & Piersol 2011) for certain cases. No difference/effect was noted in the spectra on changing the window functions. Also, since the experimental dataset is acquired by a snapshot PIV technique (i.e. not time resolved), there was no overlap in the instantaneous flow fields acquired consecutively by the PIV system. Hence, Welch's method of overlapping signals, to improve statistical convergence, could not be employed here.
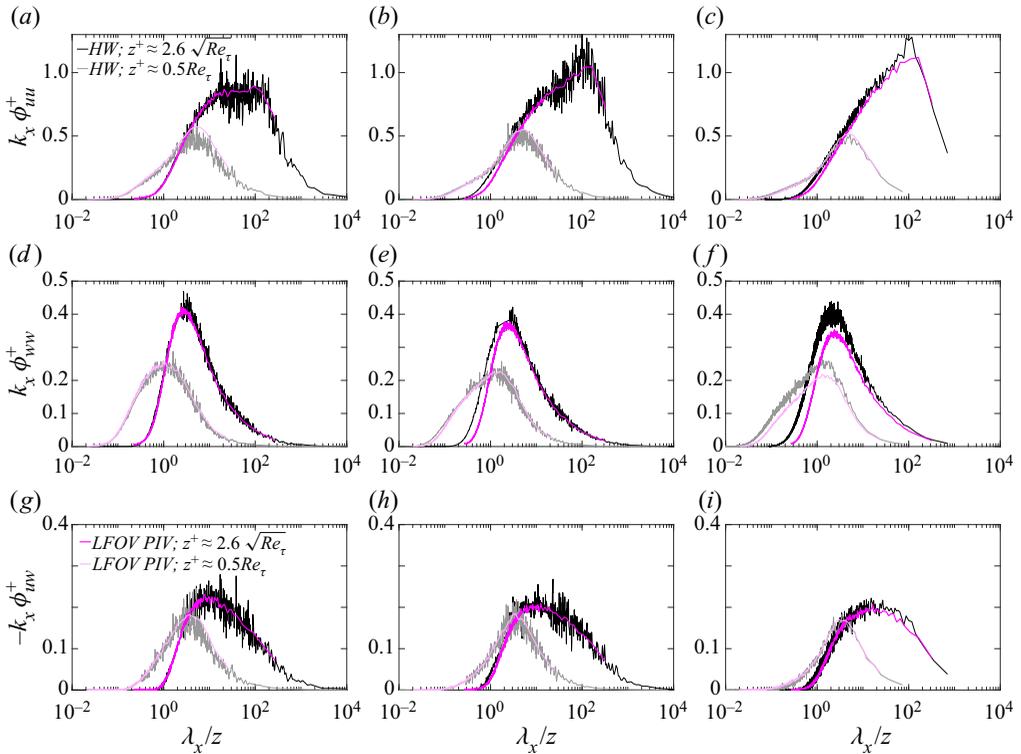
Figure 14. Premultiplied 1-D spectra of (*a–c*) *u*-fluctuations, (*d–f*) *w*-fluctuations and (*g–i*) co-spectra of the Reynolds shear stress at $Re_\tau \approx$ (*a,d,g*) 2500, (*b,e,h*) 5000 and (*c,f,i*) 7500. Lines in magenta correspond to the spectra estimated from the LFOV PIV datasets documented in table 1, while the lines in black correspond to the same computed from the multi-wire data acquired by Baidya *et al.* (2017) (at $Re_\tau \approx$ 2500 and 5000) and Morrill-Winter *et al.* (2015) (at $Re_\tau \approx$ 7500), in the same wind tunnel facility. Dark shaded lines correspond to spectra at $z^+ \approx 2.6\sqrt{Re_\tau}$, while light shaded lines correspond to $z^+ \approx 0.5Re_\tau$.

In figure 14, the spectra are plotted for $z^+ \approx 2.6\sqrt{Re_\tau}$ (nominal start of the log region) and the middle of the boundary layer ($\approx 0.5Re_\tau$), and compared against published spectra estimated from multi-wire experiments (Morrill-Winter *et al.* 2015; Baidya *et al.* 2017) conducted in the same facility and at similar Re_τ. It should be noted here that the hot-wire spectra are plotted based on the assumption of Taylor's hypothesis, with the mean velocity at z^+ considered as the mean convection velocity of the turbulent scales. Taylor's approximation has been deemed a reasonable assumption in the inertial region for $\lambda_x \lesssim 6\delta$ (Dennis & Nickels 2008; de Silva *et al.* 2015), permitting its use for validation of the PIV spectra up to this scale range. One can clearly observe that the PIV and hot-wire spectra match reasonably well, especially in the intermediate-scale range ($O(1) \lesssim \lambda_x/z \lesssim O(10)$), which nominally corresponds to the self-similar hierarchy coexisting in the boundary layer. Further, the agreement also confirms the insignificant influence of the evolution of the boundary layer thickness on the spectra, which is estimated by extracting data at a constant z-location along the x-direction. Some discrepancy at smaller λ_x is expected for high Re_τ PIV ($\sim$5000, 7500), due to relatively poor spatial resolution of PIV compared with the hot-wire sensor resolution (table 1).
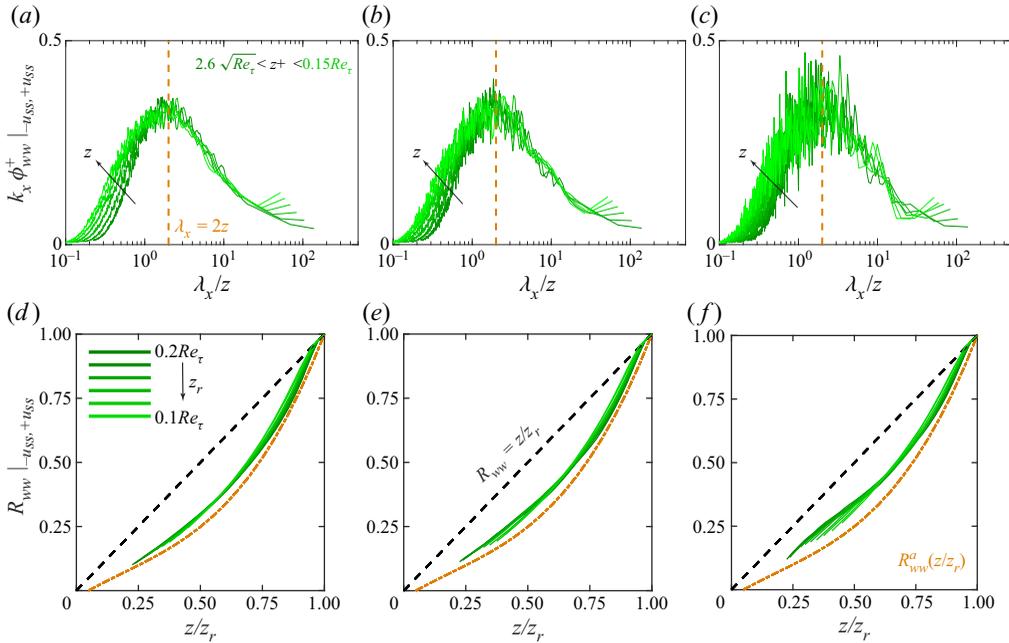
969 A10-22

Figure 15. (*a–c*) Conditionally averaged premultiplied 1-D spectra of *w*-fluctuations plotted vs λ_x/z at various z^+ within the log region. (*d–f*) Correlation between *w*-fluctuations at z and z_r, normalized by $\overline{w^2}(z_r)$ for various z_r. Here, both the spectra and the cross-correlations are computed from the extracted *w*-flow fields associated with $-u_{ss}$ and $+u_{ss}$ detected in the LFOV PIV data at $Re_\tau \approx 7500$, for varying thresholds of the streamwise lengths associated with the superstructures: (*a,d*) $L_x \gtrsim 3\delta$, (*b,e*) $L_x \gtrsim 3.8\delta$ and (*c,f*) $L_x \gtrsim 4.5\delta$. In (*a–c*), the dashed golden line represents the linear scaling, $\lambda_x = 2z$. In (*d–f*), the dashed black line corresponds to the linear relationship, z/z_r while the dash-dotted golden line corresponds to R_{ww}^a defined in (3.2).

Appendix B. Effect of thresholds on conditional statistics

Figures 15(*a*)–15(*c*) present the conditionally averaged, premultiplied *w*-spectra and figure 15(*d–f*) presents the conditionally averaged two-point correlations of the *w*-fluctuations. Both are computed from the flow fields extracted based on varying thresholds (L_x) on the streamwise extents of the identified superstructures. The statistics are computed for the $Re_\tau \approx 7500$ LFOV PIV dataset at z^+ corresponding to the log region. It is evident from the comparison that the z-scalings, exhibited by both the statistics, remain unchanged despite the change in L_x. The most prominent effect of increasing the L_x is the reduced number of ensembles (of the extracted flow fields), leading to poorly converged conditionally averaged statistics.

REFERENCES

ADRIAN, R.J., MEINHART, C.D. & TOMKINS, C.D. 2000 Vortex organization in the outer region of the turbulent boundary layer. *J. Fluid Mech.* **422**, 1–54.

DEL ÁLAMO, J.C. & JIMÉNEZ, J. 2009 Estimation of turbulent convection velocities and corrections to Taylor's approximation. *J. Fluid Mech.* **640**, 5–26.

BAARS, W.J., HUTCHINS, N. & MARUSIC, I. 2017 Self-similarity of wall-attached turbulence in boundary layers. *J. Fluid Mech.* **823**, R2.

BAIDYA, R., PHILIP, J., HUTCHINS, N., MONTY, J.P. & MARUSIC, I. 2017 Distance-from-the-wall scaling of turbulent motions in wall-bounded flows. *Phys. Fluids* **29** (2), 020712.

BAILEY, S.C.C., HULTMARK, M., SMITS, A.J. & SCHULTZ, M.P. 2008 Azimuthal structure of turbulence in high Reynolds number pipe flow. *J. Fluid Mech.* **615**, 121–138.

BALAKUMAR, B.J. & ADRIAN, R.J. 2007 Large- and very-large-scale motions in channel and boundary-layer flows. *Phil. Trans. R. Soc.* A*: Math. Phys. Engng Sci.* **365** (1852), 665–681.

BALTZER, J.R., ADRIAN, R.J. & WU, X. 2013 Structural organization of large and very large scales in turbulent pipe flow simulation. *J. Fluid Mech.* **720**, 236–279.

BENDAT, J.S. & PIERSOL, A.G. 2011 *Random Data: Analysis and Measurement Procedures*. John Wiley & Sons.

CHAUHAN, K.A., MONKEWITZ, P.A. & NAGIB, H.M. 2009 Criteria for assessing experiments in zero pressure gradient boundary layers. *Fluid Dyn. Res.* **41** (2), 021404.

COMTE-BELLOT, G. 1963 *Turbulent Flow between Two Parallel Walls*. Universite de Grenoble (translated by P. Bradshaw, Rep. ARC 31609 FM4/02, 1969).

DECK, S., RENARD, N., LARAUFIE, R. & WEISS, P. 2014 Large-scale contribution to mean wall shear stress in high-Reynolds-number flat-plate boundary layers up to 13 650. *J. Fluid Mech.* **743**, 202–248.

DEL ALAMO, J.C. & JIMENEZ, J. 2006 Linear energy amplification in turbulent channels. *J. Fluid Mech.* **559**, 205–213.

DENNIS, D.J.C. & NICKELS, T.B. 2008 On the limitations of Taylor's hypothesis in constructing long structures in a turbulent boundary layer. *J. Fluid Mech.* **614**, 197–206.

DENNIS, D.J.C. & NICKELS, T.B. 2011 Experimental measurement of large-scale three-dimensional structures in a turbulent boundary layer. Part 2. Long structures. *J. Fluid Mech.* **673**, 218–244.

DESHPANDE, R., CHANDRAN, D., MONTY, J.P. & MARUSIC, I. 2020 Two-dimensional cross-spectrum of the streamwise velocity in turbulent boundary layers. *J. Fluid Mech.* **890**, R2.

DESHPANDE, R., MONTY, J.P. & MARUSIC, I. 2021*a* Active and inactive components of the streamwise velocity in wall-bounded turbulence. *J. Fluid Mech.* **914**, A5.

DESHPANDE, R., DE SILVA, C.M., LEE, M., MONTY, J.P. & MARUSIC, I. 2021*b* Data-driven enhancement of coherent structure-based models for predicting instantaneous wall turbulence. *Intl J. Heat Fluid Flow* **92**, 108879.

GUALA, M., HOMMEMA, S.E. & ADRIAN, R.J. 2006 Large-scale and very-large-scale motions in turbulent pipe flow. *J. Fluid Mech.* **554**, 521–542.

HU, R., YANG, X.I.A. & ZHENG, X. 2020 Wall-attached and wall-detached eddies in wall-bounded turbulent flows. *J. Fluid Mech.* **885**, A30.

HUNT, J.C.R., KAIMAL, J.C. & GAYNOR, J.E. 1988 Eddy structure in the convective boundary layer-new measurements and new concepts. *Q. J. R. Meteorol. Soc.* **114** (482), 827–858.

HUNT, J.C.R., MOIN, P., MOSER, R.D. & SPALART, P.R. 1987 Self similarity of two point correlations in wall bounded turbulent flows. In *CTR Annual Research Briefs*, pp. 25–36.

HUTCHINS, N., CHAUHAN, K., MARUSIC, I., MONTY, J. & KLEWICKI, J. 2012 Towards reconciling the large-scale structure of turbulent boundary layers in the atmosphere and laboratory. *Boundary-Layer Meteorol.* **145** (2), 273–306.

HUTCHINS, N. & MARUSIC, I. 2007 Evidence of very long meandering features in the logarithmic region of turbulent boundary layers. *J. Fluid Mech.* **579**, 1–28.

HWANG, Y. & COSSU, C. 2010 Self-sustained process at large scales in turbulent channel flow. *Phys. Rev. Lett.* **105** (4), 044505.

HWANG, J. & SUNG, H.J. 2018 Wall-attached structures of velocity fluctuations in a turbulent boundary layer. *J. Fluid Mech.* **856**, 958–983.

KIM, K.C. & ADRIAN, R.J. 1999 Very large-scale motion in the outer layer. *Phys. Fluids* **11** (2), 417–422.

KLINE, S.J., REYNOLDS, W.C., SCHRAUB, F.A. & RUNSTADLER, P.W. 1967 The structure of turbulent boundary layers. *J. Fluid Mech.* **30** (4), 741–773.

LEE, J., LEE, J.H., CHOI, J. & SUNG, H.J. 2014 Spatial organization of large- and very-large-scale motions in a turbulent channel flow. *J. Fluid Mech.* **749**, 818–840.

LEE, J.H. & SUNG, H.J. 2011 Very-large-scale motions in a turbulent boundary layer. *J. Fluid Mech.* **673**, 80–120.

LEE, J.H., SUNG, H.J. & ADRIAN, R.J. 2019 Space–time formation of very-large-scale motions in turbulent pipe flow. *J. Fluid Mech.* **881**, 1010–1047.

LIU, Z., ADRIAN, R.J. & HANRATTY, T.J. 2001 Large-scale modes of turbulent channel flow: transport and structure. *J. Fluid Mech.* **448**, 53–80.

LOZANO-DURÁN, A., FLORES, O. & JIMÉNEZ, J. 2012 The three-dimensional structure of momentum transfer in turbulent channels. *J. Fluid Mech.* **694**, 100–130.

MARUSIC, I., CHAUHAN, K.A., KULANDAIVELU, V. & HUTCHINS, N. 2015 Evolution of zero-pressure-gradient boundary layers from different tripping conditions. *J. Fluid Mech.* **783**, 379–411.

MARUSIC, I. & MONTY, J.P. 2019 Attached eddy model of wall turbulence. *Annu. Rev. Fluid Mech.* **51**, 49–74.

MCKEON, B.J. & SHARMA, A.S. 2010 A critical-layer framework for turbulent pipe flow. *J. Fluid Mech.* **658**, 336–382.

MEINHART, C.D. & ADRIAN, R.J. 1995 On the existence of uniform momentum zones in a turbulent boundary layer. *Phys. Fluids* **7** (4), 694–696.

MORRILL-WINTER, C., KLEWICKI, J., BAIDYA, R. & MARUSIC, I. 2015 Temporally optimized spanwise vorticity sensor measurements in turbulent boundary layers. *Exp. Fluids* **56** (12), 216.

SABOT, J., RENAULT, J. & COMTE-BELLOT, G. 1973 Space-time correlations of the transverse velocity fluctuation in pipe flow. *Phys. Fluids* **16** (9), 1403–1405.

SILLERO, J.A., JIMÉNEZ, J. & MOSER, R.D. 2013 One-point statistics for turbulent wall-bounded flows at Reynolds numbers up to $\delta^+ \approx 2000$. *Phys. Fluids* **25** (10), 105102.

SILLERO, J.A., JIMÉNEZ, J. & MOSER, R.D. 2014 Two-point statistics for turbulent boundary layers and channels at Reynolds numbers up to $\delta^+ \approx 2000$. *Phys. Fluids* **26** (10), 105109.

DE SILVA, C.M., CHANDRAN, D., BAIDYA, R., HUTCHINS, N. & MARUSIC, I. 2020 Periodicity of large-scale coherence in turbulent boundary layers. *Intl J. Heat Fluid Flow* **83**, 108575.

DE SILVA, C.M., GNANAMANICKAM, E.P., ATKINSON, C., BUCHMANN, N.A., HUTCHINS, N., SORIA, J. & MARUSIC, I. 2014 High spatial range velocity measurements in a high Reynolds number turbulent boundary layer. *Phys. Fluids* **26** (2), 025117.

DE SILVA, C.M., HUTCHINS, N. & MARUSIC, I. 2016 Uniform momentum zones in turbulent boundary layers. *J. Fluid Mech.* **786**, 309–331.

DE SILVA, C.M., SQUIRE, D.T., HUTCHINS, N. & MARUSIC, I. 2015 Towards capturing large scale coherent structures in boundary layers using particle image velocimetry. In *Proceedings of the 7th Australian Conference on Laser Diagnostics in Fluid Mechanics and Combustion, Melbourne, Australia*.

SMITS, A.J., MCKEON, B.J. & MARUSIC, I. 2011 High–Reynolds number wall turbulence. *Annu. Rev. Fluid Mech.* **43**, 353–375.

TOWNSEND, A.A. 1976 *The Structure of Turbulent Shear Flow*, 2nd edn. Cambridge University Press.

TRITTON, D.J. 1967 Some new correlation measurements in a turbulent boundary layer. *J. Fluid Mech.* **28** (3), 439–462.

WU, X., BALTZER, J.R. & ADRIAN, R.J. 2012 Direct numerical simulation of a 30*R* long turbulent pipe flow at $R+ = 685$: large- and very large-scale motions. *J. Fluid Mech.* **698**, 235–281.